NJC

Accepted Manuscript

This article can be cited before page numbers have been issued, to do this please use: C. Zhou, J. Wang, X. Liu, F. Chen, Y. Di, S. Gao and Q. Shi, *New J. Chem.*, 2018, DOI: 10.1039/C8NJ00896E.

ROYAL SOCIETY OF CHEMISTRY

rsc.li/njc

View Article Online
DOI: 10.1039/C8NJ00896E

Magnetic and thermodynamic properties of α, β, γ and δ-MnO_2

Chunsheng Zhou[1], Jianfang Wang[1], Xin Liu[2*], Fengying Chen[1], Youying Di[1], Shengli Gao[1], Quan Shi[2*]

1 College of Chemical Engineering and Modern Materials, Shangluo University, Shangluo 726000, P. R.China;

2 Thermochemistry Laboratory, Liaoning Province Key Laboratory of Thermochemistry for Energy and Materials, Dalian National Laboratory for Clean Energy, Dalian Institute of Chemical Physics, Chinese Academy of Sciences, Dalian 116023, P. R. China

* Author for correspondence:

E-mail addresses: liuxin01@dicp.ac.cn (X. Liu); shiquan@dicp.ac.cn (Q. Shi).

View Article Online
DOI: 10.1039/C8NJ00896E

Abstract:

Four different structures of manganese dioxide particles with good dispersity were obtained by hydrothermal and co-precipitation methods. The magnetic measurement reveals that the α-MnO_2 exhibit a spin-glass like behavior below 50 K which is different from the bulk α-MnO_2. The β-MnO_2 and the δ-MnO_2 exhibit a transition from paramagnetic to antiferromagnetic state at 92 K and 20 K respectively, and the γ-MnO_2 keeps the paramagnetic state during the temperature range of measurement. Besides, the δ-MnO_2 possesses the highest magnetization while the β-MnO_2 has the lowest magnetization. The thermodynamic properties of these manganese dioxides were further studied using heat capacity measurements, and the results confirmed the magnetic transition at corresponding temperatures revealed in the above magnetic measurements. Through fitting the heat capacity curve, standard molar heat capacity, entropy and enthalpy at 298.15 K (0.1 MPa) and transition enthalpy were obtained in this work. Based on the characterization results, it is supposed that the impurity ions/molecular and vacancies are the main factors that contribute to the magnetic performance of δ-MnO_2, although the layer structure thought to be an origin of ferromagnetic interaction.

Keywords: manganese dioxides, magnetic properties, thermodynamic properties, phase transition, heat capacity,

View Article Online
DOI: 10.1039/C8NJ00896E

Introduction:

Manganese dioxides are promising materials for many technology and it may exist as several crystallographic modifications (α-, β-, γ-, ε-, and δ)[1, 2]. Due to the crystal structure largely determines the functional properties of MnO_2 materials, including their magnetic properties, electrochemical characteristics, molecular absorption and catalytic properties, many efforts have been made on preparation of the family of manganese dioxides with particular crystallographic faces and novel morphologies in the past decades[3].

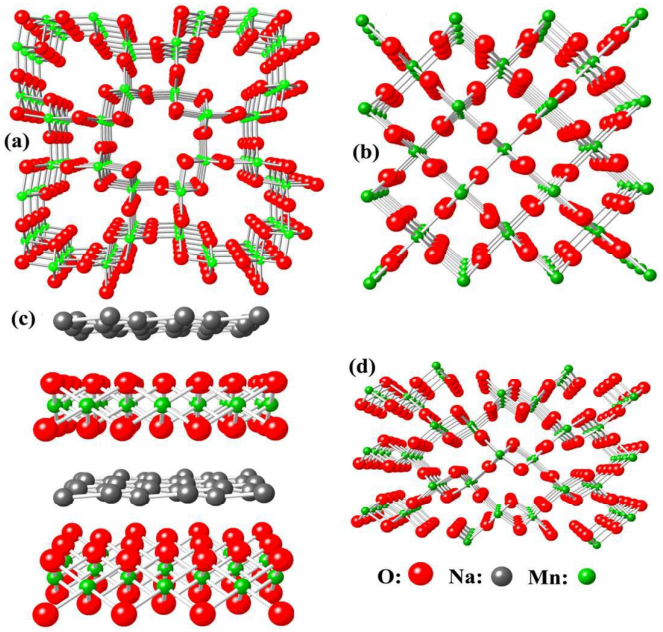

Figure 1. Schematic of phase of (a) α-MnO_2 (b) β-MnO_2 (c) δ-MnO_2 (d) γ-MnO_2

Manganese dioxides may include layered and one-dimensional tunnel units, which are composed of corner- or edge-shared MnO_6 octahedral units. For example, as the precursor material for the lithium ion batteries, an important feature of α-MnO_2 is the presence of mesoporous channels formed by the stacked MnO_6 octahedrons, as shown in Fig.1 (a), which could host K^+, Na^+, NH_4^+ or Li^+ ions to stabilize this structure.[4] The framework of these mesoporous channels, called octahedral molecular sieve structures, can form infinite alternating 1×1 and 2×2 tunnels by sharing the edges and corners of the MnO_6 octahedrons. Besides the above mentioned cationic species, neutral molecules, such as water, could also reside in the tunnels.[5] β-MnO_2 is one of the most stable manganese oxides with tunnel structure, which has

View Article Online
DOI: 10.1039/C8NJ00896E

single chains of MnO_6 edge-sharing octahedra and possesses narrow 1×1 tunnels (Fig.1 (b)).[6]

δ-MnO_2 is a layer manganese dioxide, as shown in Fig.1 (c), consisting of two-dimensional (2D) sheets of edge shared MnO_6 octahedral. Since there are electrostatic attraction or van der Waals forces existing between the inter layers, the inorganic layered materials can be delaminated into unilamellar nanosheet units with the thickness in the order of around 1 nm and the lateral size ranging from sub-micrometer to several tens of micrometers. An important characteristic of the nanosheets in all materials synthesized thus far is the presence of cation vacancies, whose negative charge is typically compensated by interlayer metal cations or portions. The layer-structured δ-MnO_2 has been widely used as cathodes for rechargeable lithium batteries and as catalysts for oxidation-reduction processes.[7, 8] For γ-MnO_2, as shown in Fig.1 (d), it has an intergrowth tunnel structure which contains β-MnO_2 domains with a relative size of (1×1) and ramsdellite domains with the size of (2×1). With larger tunnels presenting a very privileged pathway for Li-ion diffusion, the MnO_2 and its chemically formed analogues have been widely used as cathodic materials in many cylindrical and flat batteries, and have also been considered for applications in button batteries.[9]

The structural, magnetic, electrochemical and catalytic properties of these forms of bulk manganese dioxides have been previously studied by various experimental measurements and theoretical calculations.[10] For example, Manceau *et al* .analyzed different crystallographic MnO_2 samples using X-ray absorption spectroscopy for determining the local structure around the absorbing atoms materials.[11] Paik Y. *et al.* investigated the local environments and mobility of deuterons in manganese dioxide tunnel structures through variable temperature ^2H MAS NMR.[12] Strobel *et al.* employed Transmission Electron Microscopy (TEM) to study the accurate structural data and the possible correlations between structure and electrode behavior.[13] Besides, Cockayne *et al.* performed density functional theory (DFT) to investigate the magnetic property of α-MnO_2, and they also provided quantitative predictions of the short-range antiferromagnetism(AFM), an indirect bandgap, and optimal K-O distances for tunnels containing K^+, OH^-, H_2O, or H_3O^+ in this material.[14] Noda *et al*. discussed the Geometrical structures and band dispersions of α-, β-, δ-, and λ-MnO_2 crystals with collinear magnetic orders by DFT.[15] The catalytic oxidation of the formaldehyde by different crystal structures of α-, β-, δ-, and λ-MnO_2 catalysts was tested at low temperature, and the tunnel structure and active lattice oxygen species were thought to be the main

View Article Online
DOI: 10.1039/C8NJ00896E

factors of the excellent performance of δ-MnO_2.[16] The transport properties and magnetic susceptibility of single crystals of β-MnO_2 was investigated by Hirohiko Sato *et al*., and they found that the transport properties could be accompanied by a large anomaly around T_N (92 K), below which a helical magnetic long-range order could form.[17] Parida *et al.* identified and characterized various forms of manganese dioxides and observed the following sequence in the order of magnitude of the paramagnetic susceptibility values: δ- > α- > γ- > β-MnO_2 at 27 ^oC.[18]

In the last decades, a plenty of MnO_2 nanomaterials with different structures and morphologies have been synthesized and reported for their potential applications for catalytic and cathodic materials, however, the detailed study of their magnetic and thermodynamic properties have been rarely reported, especially their thermodynamic properties in the temperature range from 1.9 K to 300 K. According to the previous results, the ground state of α-MnO_2 is antiferromagnetic due to the symmetric nature of Mn-O-Mn bonds. By contrast, α-MnO_2 nanowires prepared through a hydrothermal method have been discovered to show ferromagnetic-like behavior at very low temperature,[19] and the geometrical frustration on the triangular lattices and the mixture of Mn^{3+} and Mn^{4+} ions have been considered to contribute the ferromagnetism. The magnetic properties of β-MnO_2 nanorod was investigated by Kumar et *al*. at room temperature,[20] and their study showed that the magnetic domains in nanosclaed materials could be less compared to their bulk counterparts. Also, Wang *et al*. synthesized of various MnO_2 nanostructures (α-, β-, δ-, and ε-MnO_2) and found that all the nanostructures could show a ferromagnetic-like transition at different Curie temperatures.[21] Based on these studies, it is obvious to see that the physical properties of manganese dioxides could be largely affected by the particle sizes and morphologies of materials.

To fully exploit the intrinsic properties of MnO_2 materials, a fundamental understanding of their magnetic and thermodynamic property is needed. In this contribution, we have synthesized various α, β, γ and δ-MnO_2 particles using the hydrothermal and co-precipitation method, and studied their thermodynamic and magnetic properties affected by their structures. It was found that the MnO_2 samples with different phases could present different magnetic behaviors and magnetic transitions, which were confirmed by the thermodynamic studies using the heat capacity measurement. The thermodynamic parameters and the magnetic results indicated that the water and impurities contained in the lattice may significantly affect the magnetic properties of MnO_2

View Article Online
DOI: 10.1039/C8NJ00896E

particles.

Experimental

The α-MnO_2 crystalline phase was prepared by a hydrothermal method reported by Wang *et al.*[3] In a typical procedure, 1 mmol $KMnO_4$ and 1 mmol NH_4F were dissolved in 40 mL deionized water to form a clear solution under magnetic stirring, and then this solution was transferred into a 50 mL Teflon lined autoclave. The autoclave was sealed and maintained at 150 °C for 24 h, and then cooled to room temperature naturally. The precipitates were filtered and then thoroughly washed with water. The resulting black precipitate was finally dried in an oven at 80 °C for 10 h. The β-MnO_2 was prepared by a hydrothermal method reported by Wang *et al.*[22] In a typical preparation, 3.0 mmol $MnCl_2{\cdot}H_2O$ and 3.0 mmol NaF were simultaneously dissolved in 11.0 mL deionized water and stirred for 30 min, and then a $KMnO_4$ solution (0.18 M, 11.0mL) was added into the above solution and stirred for another 30 min. The obtained slurry was then transferred into a 30 mL Teflon-lined stainless steel autoclave, sealed, and maintained at 180 °C for 36 h. The autoclave was allowed to cool to room temperature naturally. The precipitates were filtered and then thoroughly washed with water. Finally, the products were dried at 50 °C for 24 h in air.

The δ-MnO_2 was prepared by a hydrothermal method as reported by Feng *et al.*[23] A mixed solution of 0.6 M NaOH and 2 M H_2O_2 was poured quickly into a 0.3 M $Mn(NO_3)_2$ solution and stirred for 25 min. The precipitate was then subjected to hydrothermal treatment at 150 °C for 16 h in a 2 M NaOH solution, and the obtained precipitates were centrifuged and washed using deionized water for many times, and then the δ-MnO_2 was obtained by drying at 80℃ in an oven for 24 h. The γ-MnO_2 was prepared by a co-precipitation method. A solution of 8 mmol $MnSO_4$ and 8 mmol $(NH_4)_2S_2O_8$ were dissolved in 100 ml deionized water simultaneously, and the solution was then heated to 90℃ and kept at the temperature for 12 hours. When the solution was cooled down, the precipitates obtained were centrifuged and washed using deionized water for many times, followed by drying at 80℃ in an oven for 24 h.

The X-ray diffraction pattern (XRD) was measured on a D/Max2550VB+/PC diffractometer with Cu Kα radiation (λ=1.5406 Å) using an operation voltage and current of 40 kV and 40 mA, respectively. The 2θ angle ranged from 10° to 90 °with a scan step of 0.02°. The zero field cooled (ZFC) and field cooled curves were recorded from 10 K to 300 K in an applied field of 1000 Oe,

View Article Online
DOI: 10.1039/C8NJ00896E

and the hysteresis loops were measured at 5 K, 50 K and 300 K under the magnetic field up to 20 kOe, respectively, with a Vibrating Sample Magnetometer equipped in a commercial Physical Property Measurement System (PPMS). The heat capacity measurement was performed on the PPMS using a relaxation calorimetric method in the temperature range from 1.9 K to 400 K, and the measurement uncertainties were verified to be ±3% below 20 K and ±1% from 20 K to 400 K. [24] Thermogravimetric analysis (TGA) was performed on a Setaram Setsys 16/18 analyzer in a dry air with a heating rate of 10 ℃/min. The binding energy of the surface and element analysis were determined by X-ray photoelectron spectra (XPS) with an ESCALAB 250xi X-ray photoelectron spectrometer using contaminated C as internal standard (C 1s = 284.6 eV).

Results and discussion

The structures:

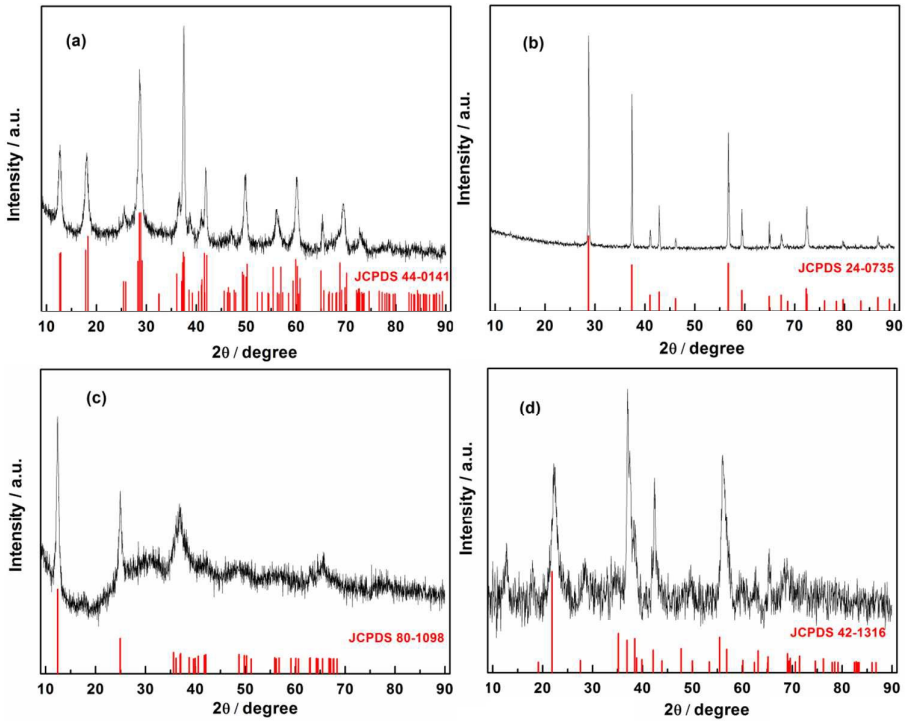

Figure 2 the X-Ray diffraction patterns of MnO_2 nanostructures: (a) α-MnO_2, (b) β-MnO_2, (c) δ-MnO_2 and (d) γ-MnO_2.

The XRD patterns of MnO_2 with different polymorphic forms are shown in Fig.2. It is observed that all of the diffraction peaks in Fig.1 (a) can be perfectly indexed to the α-MnO_2

View Article Online
DOI: 10.1039/C8NJ00896E

(JCPDS 44-0141), indicating that the α-MnO_2 crystalline phase has the space-group symmetry I4/m(87) with a body-centred tetragonal lattice type, and no other impurities are observed. The calculated lattice constants are a = 9.750 Å and c = 2.861Å. The average crystallite size estimated from peak (211) and (310) using Scherrer formula is about 93 nm. The XRD pattern of the as-prepared β-MnO_2 crystals are shown in Fig. 1(b). It can be seen that all the diffraction peaks can be easily indexed to a pure tetragonal phase (space group: $P4_2/mnm$) of β-MnO_2 with lattice constants of a = 4.399 Å and c = 2.874 Å (JCPDS 24-0735). No peaks of any other phases are detected, indicating the product has a high purity. The sharp peaks suggest the β-MnO_2 is highly crystalline and the crystallite size is near 15 μm. The δ-MnO_2 crystal has the space group symmetry $P6_3/mmc$(194) and its XRD pattern is shown in Fig1.(c). The diffraction peaks at d-values of 0.719, 0.358, 0.249, and 0.243 nm can be indexed to the birnessite (JCPDS 80-1098), and the d-values of 0.719 nm suggest that the single crystal water sheet are formed in the sodium manganese oxides.[23] The calculated crystallite size of δ-MnO_2 is about 110 nm. The XRD pattern of γ-MnO_2 is shown in Fig1.(d). The highly broadened reflections (at 22.2°, 37°, 38°, 42° and 56°) can be identified as γ-MnO_2 (JCPDS 42-1316), indicating the crystal size is smaller than others. Due to the relative low intensity of the reflection peaks, it also can be obtained that the degree of the crystallinity is low and the stresses could remain in the lattice. The calculated crystallite size of the γ-MnO_2 sample is about 40 nm. As reported, γ-MnO_2 is normally the product of intergrowth of elements of ramsdellite and pyrolusite, and thus no complete single crystal will emerge in the structure, leading to the low crystallinity of γ-MnO_2.[25]

Since the metal oxide nanoparticles tend to absorb water on their surface in air, we have performed a thermogravimetric measurement on these samples to determine the water contents in these samples. As shown in Fig.S1, the TGA curves of these four types of MnO_2 were recorded from room temperature to 1100 °C. The weight losses lower than 200 °C would be caused by the desorption of water at the surface of the crystal, while the losses at 600°C, 860°C and 490°C for these samples may correspond to the phase transformation from MnO_2 to Mn_2O_3, from Mn_2O_3 to Mn_3O_4, and from γ-MnO_2 to β-MnO_2 phase, respectively.[26-28] Considering that heating at a higher temperature would cause the phase transitions of the MnO_2, we believe that the weight loss before 400 °C is the water loss from the samples. In this regard, according the obtained results, the weights of incorporated molecular water in each sample can be calculated in their molecular

View Article Online
DOI: 10.1039/C8NJ00896E

formula form to be α-MnO_2·0.16H_2O, β-MnO_2·0.01H_2O, δ-MnO_2·0.17H_2O and γ-MnO_2·0.20H_2O.

The magnetic properties:

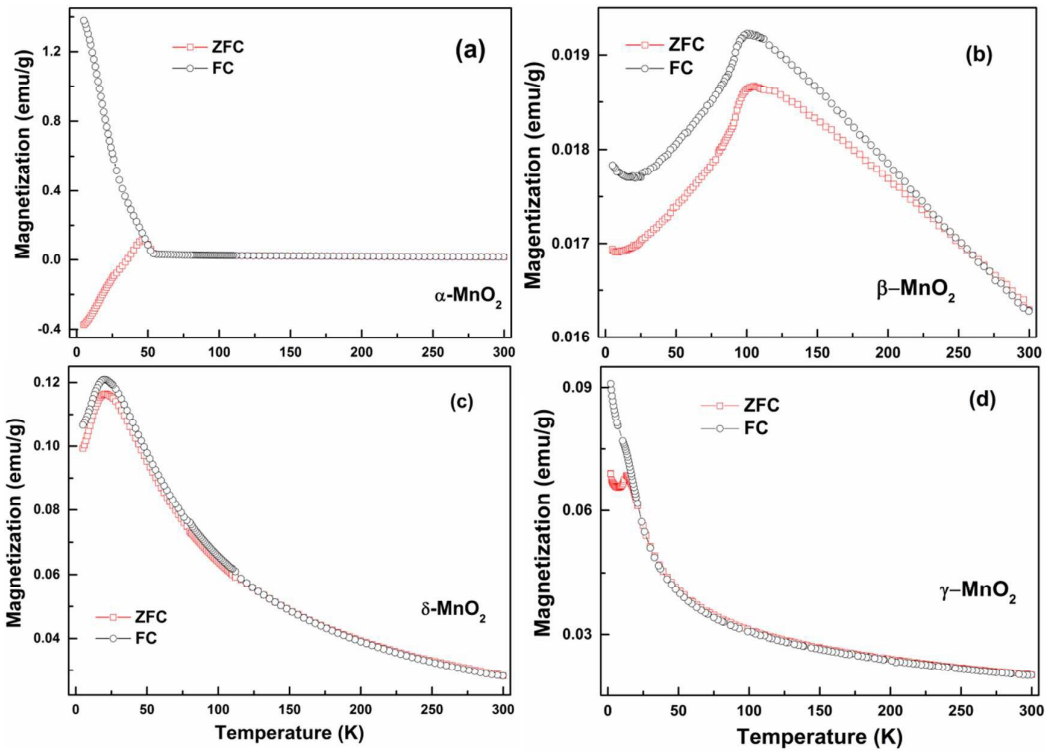

Figure 3 The ZFC and FC magnetization curves of α-MnO_2 (a), β-MnO_2 (b), δ-MnO_2 (c) and γ-MnO_2 (d) respectively.

The magnetic properties of the as-synthesized α, β, γ and δ-MnO_2 samples were investigated using the vibrating sample magnetometer on the PPMS, and the zero-field-cooled (ZFC) and field-cooled (FC) magnetization data in the range from 10 K to 300 K under 1000 Oe are presented in Fig.3. It is well known that all the oxygen octahedral in α-MnO_2 are connected to each other by point or ridge sharing, and therefore the antiferromagnetic order is preferable in this case. However, both ZFC and FC susceptibilities of the α-MnO_2 undergo a sharp rise at 52 K and diverge at lower temperatures, while they are virtually identical above 50 K, as shown in Fig.3 (a). Besides, there is a cusp on the ZFC curve at T_f = 47 K which is absent on the FC curve. This transition temperature is higher than the Neel temperature of bulk α-MnO_2(T_N =24.5 K),[29] and it

View Article Online
DOI: 10.1039/C8NJ00896E

looks like the α-MnO_2 may present an obviously ferrimagnetic transition at T =52 K. It was generally explained as the reduction in oxidation state of Mn^{4+}. Mn^{3+} existing in the lattice in order to compensate for the charge, and the distribution of Mn^{3+} and Mn^{4+} may cause a change in magnetic ground state. Similar transitions are also observed in the ions doped α-MnO_2 materials,[30, 31] and Mn_3O_4 impurity phase also could be the reason for this high hump due to its ferromagnetic transition near 50 K. The value of ZFC becomes negative when temperature is lower than 36 K, which could be caused by the negative exchange coupling among the ferromagnetic sublattices.[32] However, this transition cannot be observed in the heat capacity measurement, where a transition peak should appear at the transition temperature.

Additionally, it can be observed in Fig 3. (b) that both ZFC and FC magnetization curves showed sharp peaks at 92 K, and this profile could be concluded to show the typical antiferromagnetic behavior with the Neel temperature of 92 K. The small separation between FC and ZFC curves below T_N could be attributed to uncompensated surface spin in antiferromagnetic nanocrystals. This is in line with that β-MnO_2 crystal show a magnetic transition into helical state at 92 K, below which it has a well-known screw type incommensure magnetic structure, with the pitch of screw about 4% shorter than 7/2c.[33] Furthermore, it can be seen from Fig. 3 (c) that the ZFC and FC magnetization curves of δ-MnO_2 crystal also show peaks at 20 K, corresponding to the paramagnetic to antiferromagnetic transition, which is also confirmed by the heat capacity measurement. This transition temperature is higher than that of nano-wall of the δ-MnO_2 type found by Zhu *et al*., which has a transition at 9.2 K,[27] but lower than the transition from paramagnetic to ferromagnetic happened at 32 K in the one dimensional hierarchical layered δ-MnO_2.[34] These two curves are identical above the magnetic transition and show the feature of paramagnetic order. As for the γ-MnO_2 shown Fig.4 (d), the FC curves exhibit a typical paramagnetic character and the kink in the ZFC curves may be caused by the canted spin at the surface of the nanoparticles. With further increasing temperature from 100 K to 300 K, the magnetization of all samples tends to decrease, indicating a paramagnetic behavior happened in these samples.

View Article Online
DOI: 10.1039/C8NJ00896E

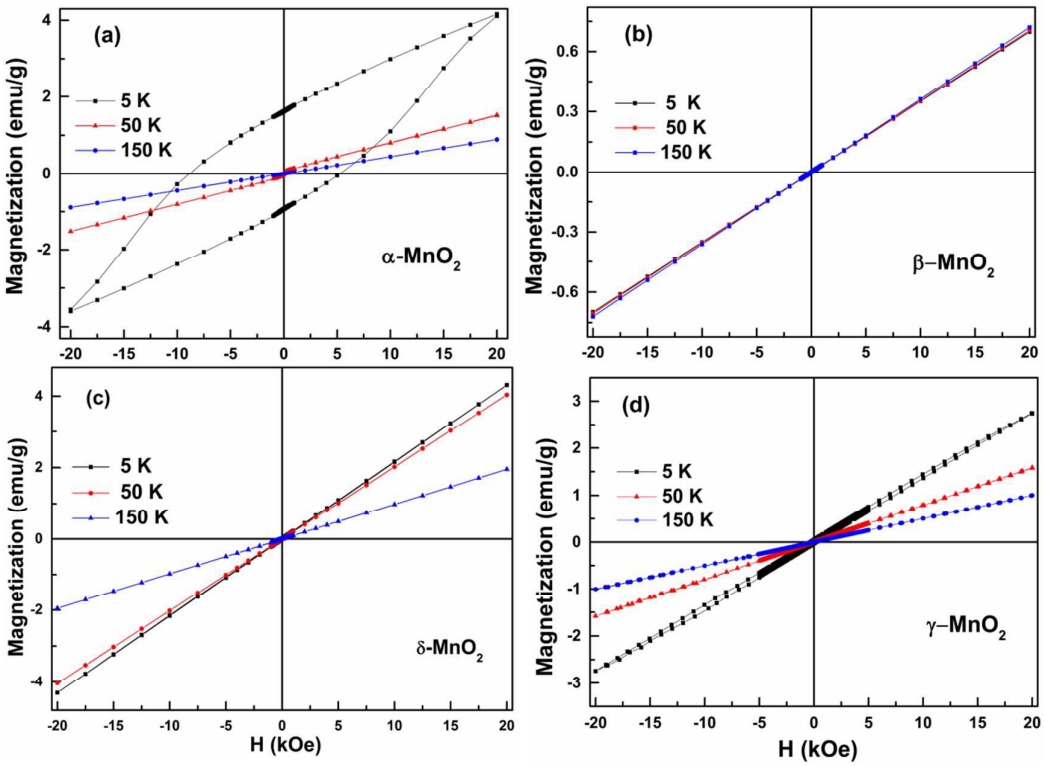

Figure 4 The isothermal field-dependent magnetization curves of α-MnO_2 (a), β-MnO_2 (b), δ-MnO_2 (c) and γ-MnO_2 (d) measured at 5 K, 50 K and 150 K, respectively.

The plots of the magnetization against the applied field for these four samples (α-MnO_2 (a), β-MnO_2 (b), δ-MnO_2 (c) and γ-MnO_2) at different temperatures are shown in Fig.4. It can be seen that, the hysteresis loop of *α*-MnO_2 (Fig.4 (b)) exhibits very small coercivities at 50 and 150 K, and the dependence of magnetization with the applied field is markedly linear and the saturation magnetization is not reached in the sample even at the maximum applied field of 20000 Oe, which could be attributed to its paramagnetic state and small anisotropy. However, the considerable hysteresis with coercivity as large as 6700 Oe can be observed at 5 K, suggesting that a magnetic transition occurred and large magnetic anisotropy exist in the α-MnO_2, and together with linear dependence at higher field values suggests a canted AFM state below T_N. In Fig.4 (b), it can be observed that the three loops of β-MnO_2 at different temperatures are all nearly linear and the coercivities are very small, and getting smaller with decreasing temperature. Based on the isothermal filed-dependent magnetization and ZFC/FC results, the β-MnO_2 should be in paramagnetic state at high temperature and change to antiferromagnetic state in the temperature

View Article Online
DOI: 10.1039/C8NJ00896E

range below 92 K.[31] The situation of δ-MnO_2 is similar with β-MnO_2, since the nearly linear M-H curves and very small coercivities suggest a paramagnetic state and a well aligned antiferromagnetic state above and below the T_N, respectively. The magnetization of γ-MnO_2 is also linear to the applied field in the measured temperatures, as presented in Fig.4 (d), indicating a paramagnetic state occurring in the temperature range from 5 K to 300 K.

In addition, the magnetization values of the MnO_2 with different polymorphic forms should be same in their paramagnetic state at 150 K. However, amongst these samples, β-MnO_2 has the lowest degree of magnetization, followed closely by sample α-MnO_2 and γ-MnO_2, and δ-MnO_2 possesses the highest magnetization. This order is similar to the previous results reported by Parida *et al.*.[18] As the temperature decreasing to 5 K, the magnetization value of δ-MnO_2, α-MnO_2 and γ-MnO_2 at 20 kOe is found to be 4.31 emu/g, 4.16 emu/g and 2.75 emu/g respectively, which are much larger than that of β-MnO_2 (0.70 emu/g), as seen from Fig.4. Several reasons can be attributed to the present observation. According to the previous theoretical results, though the interlayer magnetic interaction is weak, the ground state of the δ-MnO_2 is predicted to be ferromagnetic (FM), while the other tunneled phases are antiferromagnetic state.[10, 15] This could be caused by the different connectivity pattern linking MnO_6 octahedral between δ-MnO_2 and other phases. However, experimentally, the β-MnO_2 adopts a helical magnetic configuration and the other phases are believed to be antiferromagnetic. Except the structural factors, in δ-MnO_2, a layer charge deficit arises from the presence with layers of Mn^{3+} cations and/or vacant layer octahedral, and could be compensated by the presence of interlayer cations. The content of Mn^{3+} and defects existed in the samples has larger magnetization contribution and may intrigue the ferromagnetic interaction between the Mn ions. To evaluate the impurity ions in the δ-MnO_2 lattice, the X-ray photoelectron spectra was measured at room temperature and the results were shown in Fig. S2. This result further confirms that the Na^+ and Mn^{3+} ions existing in the lattice.

View Article Online
DOI: 10.1039/C8NJ00896E

The Thermodynamic properties:

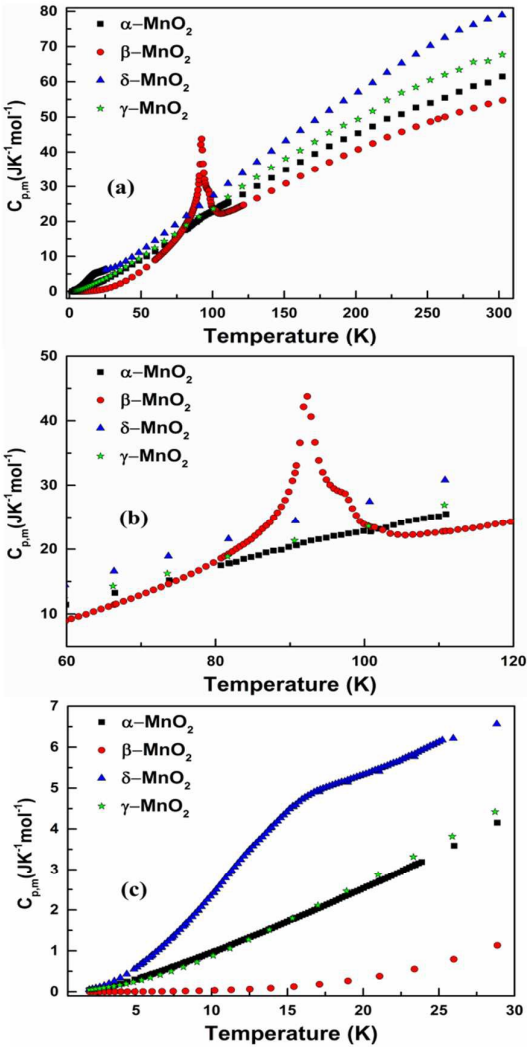

Figure 5 The heat capacity curves of α-MnO_2, β-MnO_2, δ-MnO_2 and γ-MnO_2 in the temperature range from 1.9 to 300 K(a), 60 to 120 K (b), and 1.9 to 30 K(c), respectively.

The thermodynamic property of these MnO_2 materials was studied by measuring their heat capacities using the PPMS in the temperature range from 1.9 K to 300 K. According to the TG results, we have calculated the molecular formula of these samples respectively. The molar heat capacities of these samples were therefore calculated using these molecular formula and plotted in Fig. 5 and listed in Table S-I. It can be seen from Fig.5 (a) that the heat capacities of these samples are similar at high temperatures. The differences of quantities are caused by the H_2O molecular and the impurity atoms. Also, there is a sharp anomaly in the heat capacity appear at 92 K in

View Article Online
DOI: 10.1039/C8NJ00896E

β-MnO_2, which is in good agreement with the observation of the temperature dependent magnetization measurement. Based on previous investigation, the second order phase transition appearing at 92 K in β-MnO_2 is the magnetic transition from paramagnetic to antiferromagnetic.[35] Besides, there is a broad anomaly in the heat capacity of δ-MnO_2 at 16 K, which is in agreement with results observed the magnetic measurement. However, at first glance, no obvious anomaly in the heat capacity of α-MnO_2 can be seen around the temperature where the steep increase of the susceptibilities is observed. This finding rules out long-range ferromagnetic ordering as the origin of the sharp rise in the magnetization. Besides, no peaks of impurities appeared in each curves of MnO_2 samples, such as Mn_2O_3, Mn_3O_4. Combining the magnetic and heat capacities results, we assigned the transition at $T = 47$ K to the spin glass behavior in the α-MnO_2, which may stem from the impurity ions and the vacancies.

It is well known that, the heat capacity of a substance at low temperature can be expressed as a sum of contributions closely related to lattice vibrations, electrons, magnetons, nuclei and impurities, and each property can be independently described using a proper theoretical model. Extracting these contributions by fitting the heat capacity data to theoretical models may provide important information about the physical property of the material.[36] To further understand the physical properties of the transitions, the heat capacities of these samples below 10 K were fitted to the following temperature-dependent expression,

$$C_{p,m} = A_{n\hbar}T^{-2} + \gamma T + B_3T^3 + B_5T^5 + B_{fsw}T^{3/2}e^{-\Delta/T} + n_{sch}R(\frac{\theta}{T})^2\frac{e^{\theta/T}}{(1-e^{\theta/T})^2} \qquad (1)$$

where the γT term represents the contributions from electrons or lattice defects or oxygen vacancies in the samples; the $A_{nh}T^{-2}$ term represents the contributions from the nuclear hyperfine structure; the (B_3T^3+ B_5T^5) term of odd powers in temperatures is the harmonic lattice model in terms of the lattice vibration contribution; the $B_{fsw}T^{3/2}e^{-\Delta/T}$ term represents the ferromagnetic behavior in the heat capacity; and the exponential function of $e^{-\Delta/T}$ in the magnetic terms represents a gap of spin-wave spectrum generated in an ordered magnet when anisotropy occurs. The last term in the expression is corresponding to the contribution of Schottky anomaly in this temperature region.

In the middle temperature region (10 K< T <70 K), the heat capacities were fitted to an orthogonal polynomial function shown below,

View Article Online
DOI: 10.1039/C8NJ00896E

$$C_{p,m}^0 = A_0 + A_1T + A_2T^2 + A_3T^3 + A_4T^4 + A_5T^5 + A_6T^6 + A_7T^7 + A_8T^8 \quad (2)$$

And in the high temperature region (>70 K), a combination of Debye and Einstein function was employed for the fitting,

$$C_{p,m}^0 = n_D D(\theta_D) + n_{E1}E(\theta_{E1}) + n_{E2}E(\theta_{E2}) + aT + bT^2 \quad (3)$$

where $D(\theta_D)$ and $E(\theta_E)$ are Debye and Einstein functions, θ_D and θ_E are Debye and Einstein temperatures, n_D and n_E are Debye and Einstein parameters, respectively; and the (aT+bT^2) term represents the modification for (C_v-C_p) corrections. The fitting parameters, temperature regions and corresponding percent mean-square fitting deviations (% RMS) are listed in Table S-II. It can be seen that the curve fitting % RMS of all MnO_2 samples are less than 1.98%, 0.62%, 1.0%, in the low, middle and high temperature regions, respectively, which are much smaller than the heat capacity uncertainties of 3%, from T = (1.9 to 20) K, and 1% from T= (20 to 300) K. According to the fitting parameters listed in the Table II, the antiferromagnetic contribution actually exists in the α-MnO_2 sample. Combining with the magnetic results, the transition from paramagnetic to spin-glass state should response for the sharp increase in the magnetic measurement. The T^3 contributions can also be found in the β-MnO_2 and δ-MnO_2, indicating the antiferromagnetic order at low temperature. In addition, the linear term contribution in γ-MnO_2 and δ-MnO_2 is larger than others, suggesting that more vacancies and defects should exist in their lattices, which is in accordance with XRD results.

Using the fitting parameters as well as the corresponding thermodynamic Equation (4) and (5) listed below,

$$\Delta H_0^T = \int_0^T C_{p,m}dT \quad (4)$$

$$\Delta S_0^T = \int_0^T (C_{p,m}/T)dT \quad (5)$$

the thermodynamic function were calculated in the temperature range from T = (0 to 300) K and results are given in Table S-III. The standard molar heat capacity, entropy and enthalpy at 298.15 K and 0.1MPa were determined to be $C^0_{p,m}$ = 62.34 (±0.62) J·K^{-1}·mol^{-1}, S^0_m= 62.70 (± 0.62)J·K^{-1}·mol^{-1}, H^0_m= 9.94 (±0.10) kJ·mol^{-1}; $C^0_{p,m}$ =54.29 (±0.54) J·K^{-1}·mol^{-1}, S^0_m=52.49(± 0.52) J·K^{-1}·mol^{-1}, H^0_m=8.73(±0.09) kJ·mol^{-1}; $C^0_{p,m}$=350.77(±3.5) J·K^{-1}·mol^{-1}, S^0_m=411.37(± 4.11) J·K^{-1}·mol^{-1}, H^0_m=60.210(±0.60) kJ·mol^{-1}; $C^0_{p,m}$=70.14(±0.70) J·K^{-1}·mol^{-1}, S^0_m=68.78(± 0.69) J·K^{-1}·mol^{-1}, H^0_m=11.036(±0.11) kJ·mol^{-1} for α-MnO_2, β-MnO_2, δ-MnO_2 and γ-MnO_2,

View Article Online
DOI: 10.1039/C8NJ00896E

respectively.

Conclusion:

In summary, four kinds of manganese dioxides with different structures were synthesized by the hydrothermal as well as co-precipitation methods, and the magnetic and thermodynamic properties of these four samples were investigated. It was found that the spin-glass transitions occurred in α-MnO_2 at 50 K due to the frustration, while the antiferromagnetic transition happened in β-MnO_2 and δ-MnO_2 at 92 K and 20 K respectively. The heat capacity measurement confirmed these transitions at corresponding temperature, and the thermodynamic parameters were calculated from the heat capacity measurement. These manganese dioxides enormous difference in heat capacity and magnetic properties are likely not only due to the difference of their tunnel structures, but also contributed from the water, lattice oxygen and impurity ions concentration in the lattice.

Acknowledgments:

The work was financially supported by the National Natural Science Foundation of China (Grant No. 21473198, 11775226, 21273171, 21727805, 21273100) and Liaoning Provincial Natural Science Foundation of China (Grant No. 201602741). Q. Shi would like to thank Hundred-Talent Program founded by Chinese Academy of Sciences.

Reference:

1. Thackeray, M. M. *Progress in Batteries & Battery Materials* **1995,** 14, (Lithium Ion Battery Technology), 1-85.

2. Thackeray, M. M. *Prog. Solid State Chem.* **1997,** 25, (1-2), 1-71.

3. Wang, X. H.; Ni, S. B.; Zhou, G.; Sun, X. L.; Yang, F.; Wang, J. M.; He, D. Y. *Mater. Lett.* **2010,** 64, (13), 1496-1498.

4. Post, J. E.; Vondreele, R. B.; Buseck, P. R. *Acta Crystallogr. Sect. B-Struct. Commun.* **1982,** 38, (APR), 1056-1065.

5. Kijima, N.; Ikeda, T.; Oikawa, K.; Izumi, F.; Yoshimura, Y. *J. Solid State Chem.* **2004,** 177, (4-5), 1258-1267.

6. David, W. I. F.; Thackeray, M. M.; Bruce, P. G.; Goodenough, J. B. *Mater. Res. Bull.* **1984,** 19, (1),

View Article Online
DOI: 10.1039/C8NJ00896E

99-106.

7. Aronson, B. J.; Kinser, A. K.; Passerini, S.; Smyrl, W. H.; Stein, A. *Chem. Mater.* **1999,** 11, (4), 949-957.

8. Chen, H. M.; He, J. H.; Zhang, C. B.; He, H. *J. Phys. Chem. C* **2007,** 111, (49), 18033-18038.

9. Chabre, Y.; Pannetier, J. *Prog. Solid State Chem.* **1995,** 23, (1), 1-130.

10. Franchini, C.; Podloucky, R.; Paier, J.; Marsman, M.; Kresse, G. *Phys. Rev. B* **2007,** 75, (19), 195128.

11. Manceau, A.; Combes, J. M. *Phys. Chem. Miner.* **1988,** 15, (3), 283-295.

12. Paik, Y.; Osegovic, J. P.; Wang, F.; Bowden, W.; Grey, C. P. *J. Am. Chem. Soc.* **2001,** 123, (38), 9367-9377.

13. Strobel, P.; Joubert, J. C.; Rodriguez, M. J. *J. Mater. Sci.* **1986,** 21, (2), 583-590.

14. Cockayne, E.; Li, L. *Chem. Phys. Lett.* **2012,** 544, 53-58.

15. Noda, Y.; Ohno, K.; Nakamura, S. *Physical Chemistry Chemical Physics* **2016,** 18, (19), 13294-13303.

16. Zhang, J. H.; Li, Y. B.; Wang, L.; Zhang, C. B.; He, H. *Catal. Sci. Technol.* **2015,** 5, (4), 2305-2313.

17. Sato, H.; Enoki, T.; Isobe, M.; Ueda, Y. *Physical Review B: Condensed Matter and Materials Physics* **2000,** 61, (5), 3563-3569.

18. Parida, K. M.; Kanungo, S. B.; Sant, B. R. *Electrochimica Acta* **1981,** 26, (3), 435-443.

19. Zhao, J. G.; Yin, J. Z.; Yang, S. G. *Mater. Res. Bull.* **2012,** 47, (3), 896-900.

20. Kumar, N.; Dineshkumar, P.; Rameshbabu, R.; Sen, A. *RSC Adv.* **2016,** 6, (9), 7448-7454.

21. Wang, J. Q.; Zeng, R.; Du, G. D.; Li, W. X.; Chen, Z. X.; Li, S.; Guo, Z. P.; Dou, S. X. *Mater. Chem. Phys.* **2015,** 166, 42-48.

22. Wang, J. F.; Deng, L. J.; Zhu, G.; Kang, L. P.; Lei, Z. B.; Liu, Z. H. *Crystengcomm* **2013,** 15, (34), 6682-6689.

23. Feng, Q.; Sun, E. H.; Yanagisawa, K.; Yamasaki, N. *J. Ceram. Soc. Jpn.* **1997,** 105, (7), 564-568.

24. Dai, R. X.; Zhang, S. H.; Yin, N.; Tan, Z. C.; Shi, Q. *J. Chem. Thermodyn.* **2016,** 92, 60-65.

25. Turner, S.; Buseck, P. R. *Science* **1979,** 203, (4379), 456-458.

26. Kim, S. H.; Kim, S. J.; Oh, S. M. *Chemistry of Materials* **1999,** 11, (3), 557-563.

27. Zhu, H. T.; Luo, J.; Yang, H. X.; Liang, J. K.; Rao, G. H.; Li, J. B.; Du, Z. M. *J. Phys. Chem. C*

View Article Online
DOI: 10.1039/C8NJ00896E

2008, 112, (44), 17089-17094.

28. Abdul Azim, A. A.; Kolta, G. A.; Askar, M. H. *Electrochimica Acta* **1972,** 17, 291-302.

29. Yamamoto, N.; Endo, T.; Shimada, M.; Takada, T. *Japanese Journal of Applied Physics* **1974,** 13, (4), 723-724.

30. Hashem, A. M.; Abuzeid, H. M.; Narayanan, N.; Ehrenberg, H.; Julien, C. M. *Mater. Chem. Phys.* **2011,** 130, (1-2), 33-38.

31. Barudzija, T.; Kusigerski, V.; Cvjeticanin, N.; Sorgic, S.; Perovic, M.; Mitric, M. *J. Alloy. Compd.* **2016,** 665, 261-270.

32. Kumar, A.; Yusuf, S. M. *Phys. Rep.-Rev. Sec. Phys. Lett.* **2015,** 556, 1-34.

33. Regulski, M.; Przenioslo, R.; Sosnowska, I.; Hoffmann, J. U. *Phys. Rev. B* **2003,** 68, (17), 172401.

34. Ge, J.; Zhuo, L.; Yang, F.; Tang, B.; Wu, L.; Tung, C. *Journal of Physical Chemistry B* **2006,** 110, (36), 17854-17859.

35. Ohama, N.; Hamaguchi, Y. *J. Phys. Soc. Jpn.* **1971,** 30, (5), 1311-1318.

36. Gopal, E. S. R., *Specific Heats at Low Temperatures (International Cryogenics Monograph Series)*. 1966; p 226 pp.